

See discussions, stats, and author profiles for this publication at: <https://www.researchgate.net/publication/231650446>

Electronic Structures of Manganese-Doped Rutile TiO₂ from First Principles

ARTICLE *in* THE JOURNAL OF PHYSICAL CHEMISTRY C · OCTOBER 2008

Impact Factor: 4.77 · DOI: 10.1021/jp8043797

CITATIONS

60

READS

64

1 AUTHOR:



Guosheng Shao

University of Bolton

191 PUBLICATIONS 2,707 CITATIONS

SEE PROFILE

Electronic Structures of Manganese-Doped Rutile TiO₂ from First Principles

G. Shao*

Centre for Materials Research and Innovation, University of Bolton, Bolton BL3 5AB, U.K.

Received: May 18, 2008; Revised Manuscript Received: August 25, 2008

DFT (density functional theory) calculations have been carried out to determine the effects of Mn doping to the energy band structures of rutile TiO₂, using the latest improved exchange correlation functional of Wu and Cohen. According to calculations performed on pure rutile, the use of the Wu–Cohen functional leads to improved accuracy in terms of energetic and crystallographic data and energy gap. The Mn effect on energy band structure depends on its occupancy sites in the rutile lattice. Mn substitution of the Ti sites induces significant spin polarization and effective reduction of the energy gap of rutile, with the energy gap being continuously reduced with increasing Mn doping level. Also, quality intermediate energy bands are introduced by moderate levels of substitutional Mn doping, indicating the promise to make use of a wide spectral range of solar irradiance in the visible light regime. On the other hand, interstitial Mn doping results in localized state in the forbidden band, without inducing spin polarization. Oxygen vacancy associated with substitutional Mn leads to similar effects on band structure as that associated with Ti atoms, generating localized defect levels in the forbidden band. Spin polarization can be enhanced by oxygen vacancies associated with the substitutional Mn atoms. The results of this work also indicate the likely potential in using substitutional Mn doping for spintronic applications such as nonvolatile random access memory.

1. Introduction

Two of the most pressing tasks for the modern society are to develop new renewable energy technologies and to improve the living environment. These have been the driving force for extensive exploration of TiO₂ phases (rutile and anatase) as generic smart materials, since they have the potential to deliver desirable solutions to both tasks, via a wide range of possible applications including low-cost solar cells,^{1,2} photocatalytic applications such as water splitting for H₂ production, self-cleaning or antimicrobial surfaces, and purification of water or air.^{3–7} However, such potential applications are seriously limited by the intrinsic wide energy gaps of TiO₂ phases (3.0 eV for rutile⁸ and 3.2 eV for anatase⁹), which confines the advantages of the TiO₂ phases to be viable only under ultraviolet (UV) radiation, as the UV spectral region only accounts for less than 5% of the whole solar spectrum and can be readily absorbed even by clear glass, pure water, fog or clouds. Such fundamental limitation due to the wide energy gaps of TiO₂ phases makes the material rather ineffective for most potential applications. Therefore, the potential of the TiO₂ phases cannot be effectively utilized, unless one can achieve significant reduction of the energy gaps of the materials to allow them function under visible light.

In order to address the UV limitation, a great deal of experimental work has focused on doping TiO₂ with both transition metal and nonmetal dopants.^{4,7} Theoretical investigations have also been carried out to study the energy band structures of TiO₂ phases including anatase^{8–13} and rutile.^{12–19} The rutile phase, which is the stable form of TiO₂, exhibits a direct band structure, while the band structure of the metastable anatase phase is indirect in nature. The experimentally measured energy gap of rutile is slightly narrower than that of anatase. As is well recognized, direct-gap materials usually have significantly higher optical absorption coefficient and better

optoelectronic coupling than their indirect-gap counterparts. This suggests that rutile may be promising for large area photonic applications such as low-cost and long-life solid-state photovoltaic cells.

Defects may play an important role in technological applications of TiO₂, via altering the electronic and optical properties. For example, naturally occurring rutile is almost always slightly reduced, leading to a pronounced color change of the crystal, from transparent to light and dark blue, which is accompanied by increased electrical conductivity.²⁰ Mn has been used to dope TiO₂ for photocatalytic applications, showing the effects to make the materials catalytically active under visible light.^{4,21,22} Such investigation has been mainly on the enhancement of the photocatalytic activity, with anatase being the focus of interest. Although the rutile phase is the equilibrium form of the TiO₂ material, little has been done to quantify whether effective redshift has been caused by Mn doping of pure rutile, and no effort has been made for a theoretical characterization of the Mn effects on its energy band structure. In this theoretical attempt, we aim to study the energy band structures of rutile TiO₂ that is doped with the 3d transition metal Mn. Using the density functional method, the work focuses on the Mn effects associated with varied doping sites and defects, in order to offer some *fundamental insight to guide effective doping* of rutile with Mn. The results suggest that it is important to introduce Mn at appropriate lattice sites, in order to achieve significant redshift in energy gap. The phenomenon of spin polarization associated with doping and defects will also be investigated.

2. Computational Method

Calculations in this work have been performed under the framework of the density functional theory (DFT), which states that all ground-state properties are functionals of the charge density ρ .²³ The only inaccurate term in the DFT methods lies in the formalism of the exchange-correlation energy, which requires some approximation for the method to be computa-

* E-mail: G.Shao@bolton.ac.uk.

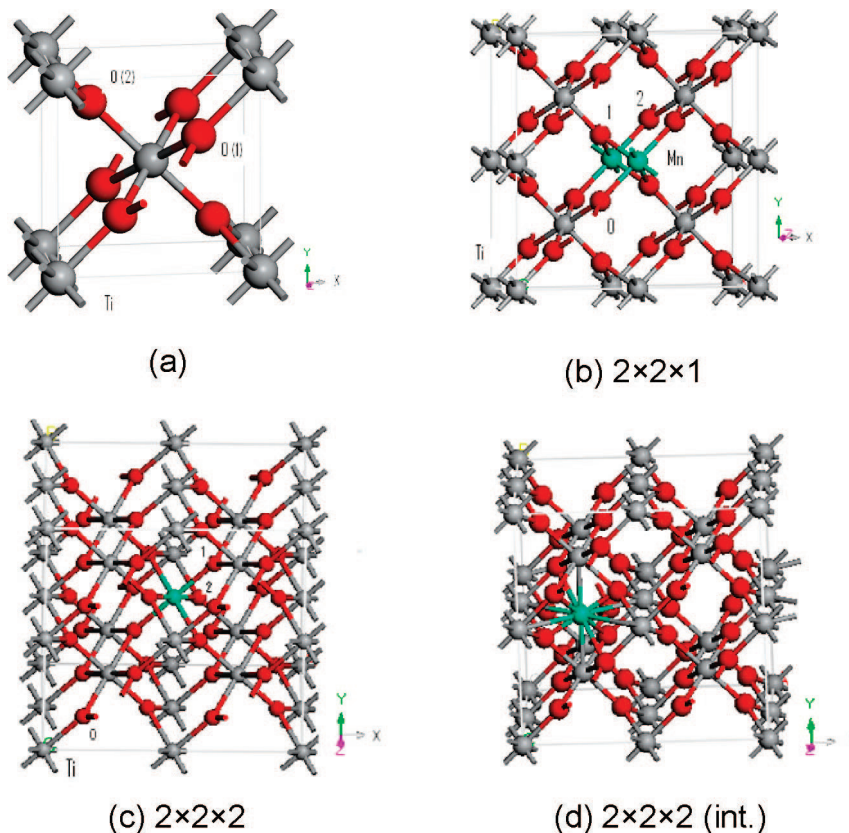


Figure 1. Crystal models: (a) unit cell of rutile TiO_2 with each Ti atom (gray) bonded to four nearest neighbor, O(1), and two second nearest neighbor O atoms (red), O(2); (b) $2 \times 2 \times 1$ supercell with a Ti atom being substituted by Mn; (c) $2 \times 2 \times 2$ supercell with a Ti atom substituted by Mn (green); (d) $2 \times 2 \times 2$ supercell with an interstitial Mn atom, which sits at the center of an octahedron made of Ti atoms.

tionally tractable. The calculation in this work has been carried out using the well tested CASTEP code,²⁴ which employs plane-wave basis sets to treat valence electrons and pseudopotentials to approximate the potential field of ionic cores (including nuclei and tightly bond core electrons).²⁵ The generalized gradient approximation (GGA) functionals have been used throughout this work, as they usually provide a better overall description of the electronic subsystem than the local density approximation (LDA) functionals. As is well-known, DFT is accurate when the exchange-correlation (XC) functional can be accurately formulated, with the exchange part usually being dominant. In this work, the latest improvement of the exchange functional by Wu and Cohen²⁶ is used together with the PBE description²⁷ of the correlation functional (PBE-WC).

Structural optimizations are performed with the Brillouin zone sampling being limited to the Γ point. For the calculations of electronic structures, the Brillouin zone is sampled by the Monkhorst–Pack grid²⁸ with k point spacing being maintained not to be more than 0.04 \AA^{-1} , to obtain the accurate density of the electronic states. This corresponds to $5 \times 5 \times 8$ k point grids for the rutile unit cell, $3 \times 3 \times 8$ grids for the $2 \times 2 \times 1$ supercell, $3 \times 3 \times 4$ grids for the $2 \times 2 \times 2$ supercell, and $3 \times 3 \times 3$ grids for a $2 \times 2 \times 3$ supercell. Test calculations show that using more k points does not lead to evident changes in the energetic convergence, electronic band structures and density maps for the electronic states. An energy cutoff of 400 eV is used. The energetic convergence threshold for self-consistent field (SCF) is 2×10^{-6} eV/atom, and atomic relaxation is carried out until all components of the residual forces are less than 0.01 eV/ \AA .

Following the well accepted convention of alloy thermodynamics, the energy of formation (E_f) of compound structures is

referred to the pure substances, i.e., the A3 structure of Ti, the α -Mn, and the oxygen molecule, so as to demonstrate whether and how much a compound structure is favored over its constituent elements. E_f in this form is widely accepted to formulate common reference for phase diagram calculations and handbook data on alloying thermodynamics.²⁹ Due to the periodic boundary condition required by CASTEP calculations, two oxygen atoms are placed within a cubic lattice with a lattice parameter of 20 \AA and the interval between the two oxygen atoms being the molecular bond length. Geometric optimization is carried to relax the elemental reference structures. The relaxed oxygen bond lengths are 1.239 and 1.224 \AA , using the PBE and PBE-WC potentials, respectively, the latter being in improved agreement with the experimentally measured value of 1.21 \AA .³⁰ For a lattice containing x titanium atoms, y manganese atoms and z oxygen atoms, the energy of formation is given by

$$E_f = E_{\text{Ti}_x\text{Mn}_y\text{O}_z}^{\text{tot}} - [x\mu_{\text{Ti}} + y\mu_{\text{Mn}} + z\mu_{\text{O}}] \quad (1)$$

where $E_{\text{Ti}_x\text{Mn}_y\text{O}_z}^{\text{tot}}$ refers to the total energy of the compound, and μ_i refers to the atomic total energy of the reference element i .

3. Results and Discussion

3.1. Pure Rutile. The unit cell of rutile TiO_2 is tetragonal with $a = 4.594 \text{ \AA}$ and $c = 2.959 \text{ \AA}$, as is shown in Figure 1a. The structure parameter of rutile, u , is 0.305. Each Ti atom is bonded to four nearest and two second nearest oxygen neighbors. The corresponding Ti–O bond lengths with the nearest and second nearest oxygen atoms are slightly different (1.949 vs 1.980 \AA).³¹ Before band structure calculation, the rutile

TABLE 1: Comparison between Calculated Structural, Energetic, and Electronic Data, with Experimental and Theoretical Data in the Literature

structural data							
<i>a</i> (Å)	<i>c</i> (Å)	<i>u</i>	Ti–O (1) (Å)	Ti–O (2) (Å)	<i>E_g</i> (eV)	<i>E_f</i> (eV/atom)	note
4.6472	2.9667	0.305	1.9599	2.0051	1.87	-3.389	GGA: PBE
4.5982	2.9461	0.305	1.9466	1.9789	2.03	-3.188	GGA: PBE-WC
4.594 ^a	2.959 ^a	0.305 ^a	1.947 ^a	1.980 ^a	3.0 ^b	-3.26 ^c	experimental
					1.87 ^d		LDA
					2.0 ^e		LDA
					1.9 ^f		GGA
					1.85 ^g		GGA

^a From ref 31. ^b From ref 8. ^c From ref 29. ^d From ref 18. ^e From ref 17. ^f From ref 19. ^g From ref 14.

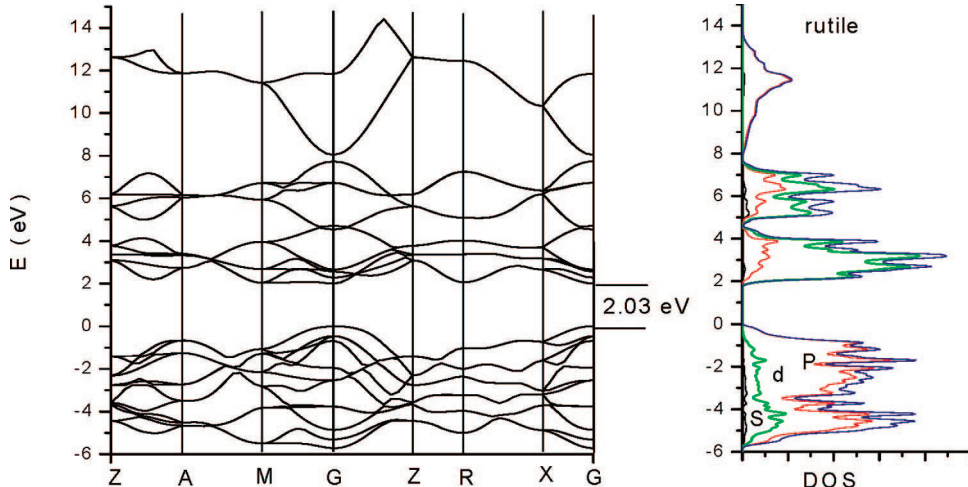


Figure 2. Band structure and DOS for pure rutile. DOS shows that the top of the valence band is dominated by the oxygen 2p states and the bottom of the conduction band is dictated by the titanium 3d states.

structure was fully relaxed using both the PBE and the PBE-WC functionals, and the resultant data are listed in Table 1 to compare with available experimental and theoretical data.

The calculated crystallographic data and the energy of formation for rutile are in excellent agreement with experimental values.^{31,29} The overall characteristics of the energy band structure calculated in this work is consistent with previous investigations,^{14–19} showing a direct energy gap at the Γ point (G), Figure 2. The energy density of states (DOS) reveals that the bottom of the conduction band (CB) is dictated by the Ti 3d electron states and the top of the valence band (VB) dominated by the oxygen 2p electron states. The use of the PBE-WC functional results in improved accuracy in terms of lattice parameters, Ti–O bond lengths, energy of formation, and the energy gap, with respect to those due to the PBE functional. It is worth noting that the improvement in the energy gap due to the PBE-WC functional is still limited, with the calculated energy gap considerably smaller than the experimental value. As is well-known, DFT calculation usually underestimates the energy gap of oxide semiconductors.^{10–19} However, this will not affect the discussion of this work, which is mainly interested in the relative change in the rutile energy gap due to Mn doping, with or without associating the dopant with oxygen vacancies.

3.2. Mn Substitution of Ti Lattice Site. To study the doping effect, we introduce a Mn atom into the $2 \times 2 \times 1$ (24 atoms), $2 \times 2 \times 2$ (48 atoms) and $2 \times 2 \times 3$ (72 atoms) supercells of rutile, to substitute a Ti atom. As examples, the first two supercells are shown in Figure 1b and c. This leads to different levels of doping with Mn accounting for 1/8, 1/16, and 1/24 of the Ti lattice sites. The substitutional Mn atom is placed either at the body-centered Ti site or the base-centered Ti site in a

supercell (To assist those who are unfamiliar with crystallography, only half of each base-centered atom belongs to the doped supercell). Such a substitution scheme helps reduce the distortion of the tetragonal lattice through full structural relaxation. It is worth pointing out that the choice of these supercell configurations to address the doping level is adequate in term of cell sizes. Test calculations reveal ignorable effect due to the artificial interaction between images. For example, for a substitutional Mn content of 1/8 Ti sites, one can either use a $2 \times 2 \times 1$ supercell containing one Mn atom, or use a $2 \times 2 \times 2$ supercell containing two Mn atoms. Using the same SCF convergence threshold, test calculations show negligible discrepancy between the two cases, with ignorable total energy difference of less than 2×10^{-5} eV/atom.

The lattice parameters of the relaxed MnO₂ phase of the rutile structure are $a = 4.8533$ Å, $c = 2.8844$ Å, with the Mn–O (1) and Mn–O (2) bond lengths being 1.82311 and 2.3165 Å, respectively (Table 2). Comparing to the TiO₂ rutile phase (Table 1), the Mn–O (1) bond length is about 0.1 Å shorter (1.8231 vs 1.9466 Å) and the Mn–O(2) bond length is considerably longer (2.3165 vs 1.9789 Å). The lattice parameters of the relaxed supercells are summarized in Table 2. The change in the Mn–O bond lengths and the lattice parameters are consistent with the reference binary structures, such that the Mn–O(2) bond lengths in the supercells fall between those of the pure TiO₂ and MnO₂.

According to the data summarized in Tables 1 and 2, the energy of formation for the Mn doped rutile supercells are less negative than that for the virgin rutile phase, this being consistent with the fact that the oxygen affinity of Mn is lower than that of Ti. The measured standard energy of formation for MnO₂ is

TABLE 2: Calculated Structural and Energy Band Data for Mn Doped Rutile Supercells under Spin-Polarized Condition

structural model	lattice parameters for fully relaxed structure										intermed gap (eV)	defect levels (eV)	magnetic moment (μ_B)
	Mn–O (1) (Å)	Mn–O (2) (Å)	a (Å)	b (Å)	C (Å)	α (deg.)	β (deg.)	γ (deg.)	E_f (eV/atom)	E_g (eV)			
2 × 2 × 3 sub.	1.9207	1.9411 ^a	9.1875	9.1875	8.8413	90.0	90.0	90.11	-2.9493	1.81	E_U 0.21 E_L 1.23	—	3.4511
2 × 2 × 2 sub.	1.9302	1.9441	9.2113	9.2113	5.8812	90.0	90.0	90.10	-2.5681	1.01	—	—	3.4406
2 × 2 × 1 sub.	1.9040	1.9747	9.2032	9.2032	2.9363	90.0	90.0	90.06	-2.4835	0.76	—	—	3.2956
2 × 2 × 2 int.			9.3279	9.2543	5.8996	90.0	90.0	89.52	-2.5717	2.31	—	CB-0.56 CB-0.97 CB-1.29	0.0093
2 × 2 × 2 sub. + vac (1)			9.2951	9.2950	5.9051	90.48	89.52	93.05	-2.4835	2.11 ^b	—	CB-0.10	3.9728
											CB-0.21 CB-0.82 VB+0.16 VB+0.28 VB+0.52		
2 × 2 × 2 sub. + vac (2)			9.2643	9.2643	5.9294	89.45	89.45	87.79	-2.4721	1.96	—	CB-0.13	5.0056
											CB-0.82 VB+0.22 VB+0.55		

^a The lattice parameter of MnO₂ of the rutile structure are $a = 4.8533 \text{ \AA}$ and $c = 2.8844 \text{ \AA}$, with the Mn–O (1) and Mn–O (2) bond lengths in relaxed MnO₂ of the rutile structure being 1.8231 and 2.3165 Å, respectively. ^b The energy of formation for the 2 × 2 × 2 rutile supercell with vac(1) is -2.4830 eV/atom.

-1.797 eV/atom (vs -3.188 eV/atom for rutile TiO₂),²⁹ and the calculated energy of formation for the metastable rutile structure of MnO₂ is about half of that for the stable phase (-0.809 eV/atom). Therefore, increased Mn doping level results in positive change in the energy of formation, such that E_f increases from -3.188 eV for pure rutile up to -2.4835 for the doping level with 1/8 Mn substitution of Ti. The energy of formation of doped supercells is all more negative than that of the pure MnO₂, suggesting higher stability of Mn doped rutile supercells with respect to the MnO₂ phase. It should be mentioned that it is necessary to calculate the Ti–Mn–O phase diagram for one to work out the equilibrium thermodynamic limit for doping, as equilibrium alloying/doping levels are determined by the relative stabilities of rival phases including those in the Mn–O binary system. For the case of substituting Ti by Mn, the thermodynamic assessment involves Gibbs energy formulation of the compositional region covering TiO₂, MnO₂, and Mn₃O₄. Such extensive energetic analysis is beyond the scope of the present work.

It is observed that spin polarization plays an important role for the energy band structures of substitutional Mn-doped rutile. Without spin polarization, there exist intermediate energy bands/states near the middle of the forbidden band. These intermediate bands are raised toward the bottom of the CB under the spin polarized condition, with the top of the VB being raised up to the Fermi level. The spin polarized band structures for the 2 × 2 × 1, 2 × 2 × 2, and 2 × 2 × 3 supercells with a substitutional Mn atom are shown in Figure 3. It is obvious that substitutional Mn doping significantly affects the energy band structure. First, substitutional Mn causes effective reduction in the energy gap. At lower dopant content (e.g., 2 × 2 × 3 supercell), intermediate energy bands/states are introduced near the bottom of the conduction band. Increasing dopant content widens the intermediate bands to make them join the conduction band, making the energy gap continuously tuneable through replacing Ti lattice sites by increased Mn content.

Contrary to claims that some transition metal doping leads to highly localized defect levels in the forbidden band in anatase

TiO₂,¹⁴ the intermediate bands owing to Mn substitution of Ti demonstrate considerable curvatures, indicating good electron mobility within them. The presence of intermediate bands separates the energy gap into the wider lower gap and the significantly narrower upper gap. At a moderate doping level, e.g., ~4 at % of the Ti sites in the 2 × 2 × 3 supercell (72 atoms), the lower intermediate energy gap, E_L , is only 61% of the energy gap of the pure rutile phase, and the upper intermediate gap, E_U , is only 10% of the rutile energy gap, making E_L the controlling gap for carrier production under photon radiation. For a substitutional doping level of 1/8 Ti site, the total energy gap is narrowed by about 63%, and for 1/16 Ti substitution, the energy gap is narrowed for about 50%. Therefore, in the range of doping level investigated in this work, the redshift in the energy gap can push the material to function in the boundary region between the red and infrared regime of the solar spectral irradiance.

To the author's knowledge, no experimental characterization has been performed to measure the energy gaps of Mn-doped rutile TiO₂. Such experimental exploration is highly desirable, as significant redshift in the rutile energy gap offers great promise in using the material in various applications. The presence of curved intermediate energy bands at moderate doping level also makes it probable to make solar cells of high energy conversion efficiency, due to the ability to absorb a wider range of solar spectral radiation that spans incident photons with energy higher than E_L , E_U and $E_L + E_U + \Delta E_I$ (ΔE_I refers to the width of the intermediate band). The intermediate bands offer "stepping stones" for the absorption of low energy photons, via the excitation of electrons at the VB top to the intermediate bands, from where they can be excited again above the CB bottom for effective PV energy conversion. The significant curvatures of the intermediate bands/states permit enhanced carrier separation, as mobile electrons of varied energetic states within them can offer enhanced electron conductivity together with improved optical absorption.

The intermediate energy bands mainly originate from the Mn 3d electrons. As an example, this is demonstrated in Figure 4,

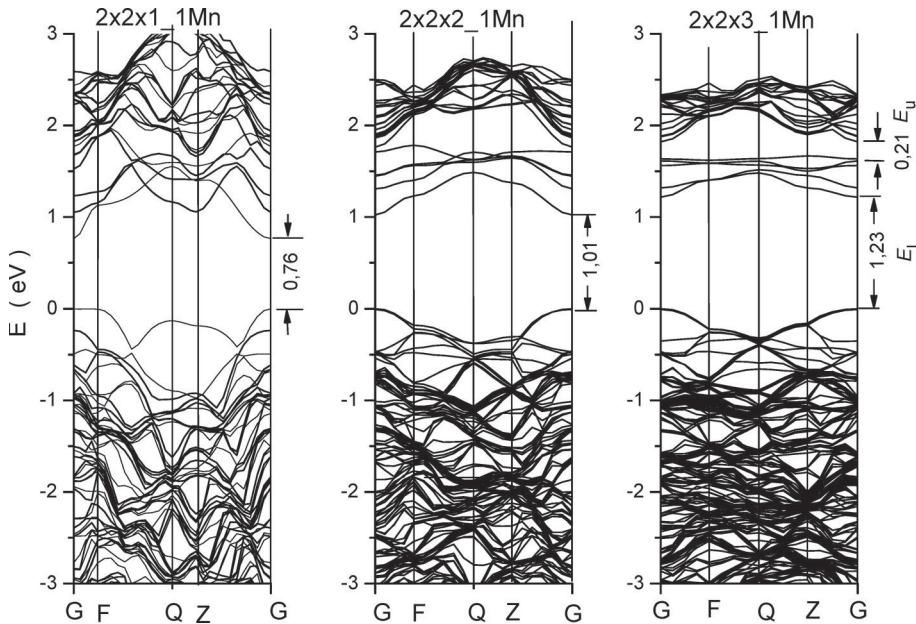


Figure 3. Spin polarized band structures for rutile supercells with a Ti atom replaced by Mn in (a) the $2 \times 2 \times 1$, (b) the $2 \times 2 \times 2$, and (c) the $2 \times 2 \times 3$. The corresponding Mn contents are 12.5%, 6.25%, and 4.17 at% of the Ti lattice sites.

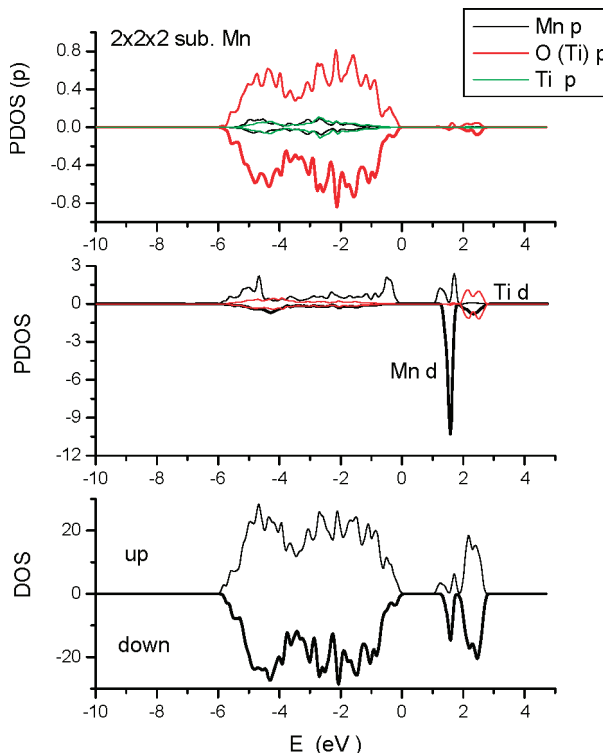


Figure 4. Full and atomic partial density of states (DOS and PDOS) for $2 \times 2 \times 2$ supercell containing a substitutional Mn atom. The intermediate bands next to the bottom of the conduction band are mainly attributed to Mn d electrons. The top of valence band is dominated by oxygen p state. The O p PDOS refers to that bonded to Ti, which is representative to the majority of O atoms. O atoms bonded to Mn demonstrate spin polarization.

which presents the spin-polarized density of states, both full (DOS) and atomic partial (PDOS), for the substitutional Mn doped $2 \times 2 \times 2$ supercells. The up and down spins are evidently differentiated and the induced intermediate bands/states correspond to the Mn 3d states. Similar to the case of pure rutile, the conduction band is dominated by the 3d states, and oxygen 2p electrons dictate the valence band. The up/down-

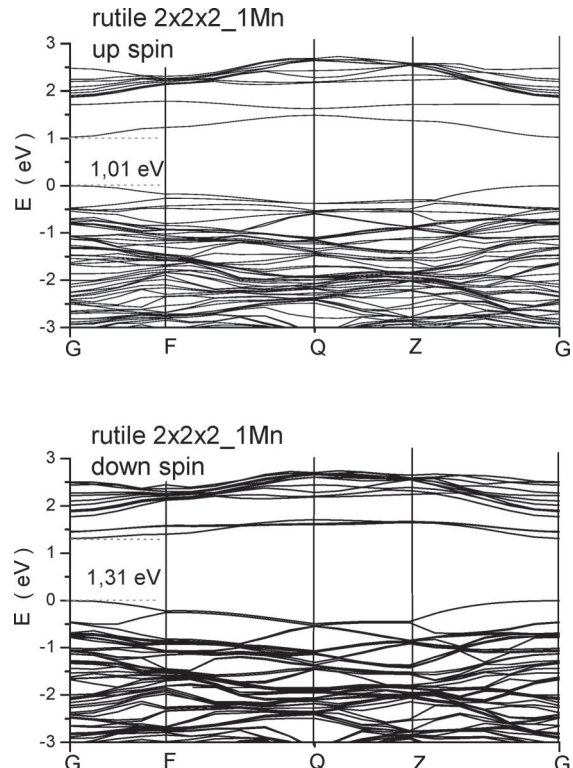


Figure 5. Up (a) and down (b) spin polarized band structures for the $2 \times 2 \times 2_1\text{Mn}$ rutile supercell.

spin induced band structures corresponding to Figure 3b are shown in Figure 5, suggesting that the intermediate gaps are dictated by the up spin of Mn 3d states (It is known that DFT alone cannot predict energy gap accurately, due to the approximation in the XC potentials. While the accuracy in the calculated energy gap can be improved to a certain extent by the introduction of an effective Hubbard U to count for the localized electron interactions, particularly for the d and f electrons, there are no accepted rules for the choice of the value of the U parameter. Our calculation using the DFT-U method showed overall agreement with the DFT method on the redshift

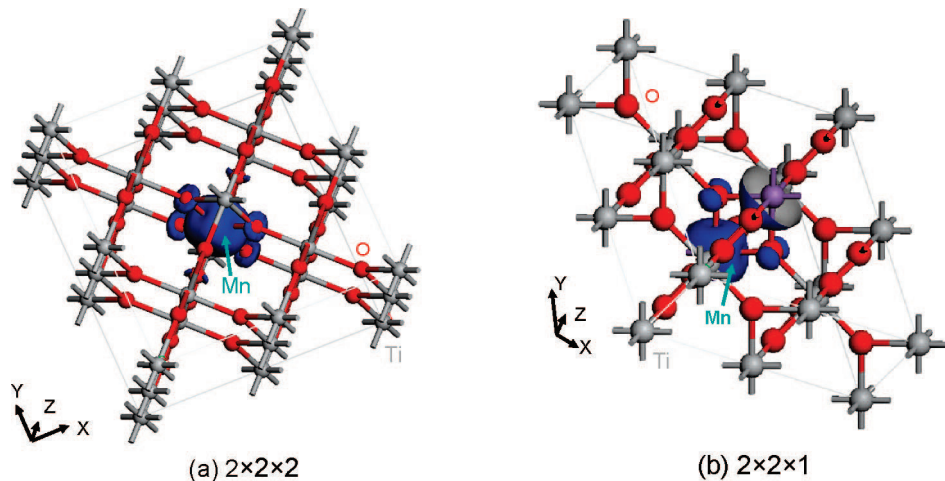


Figure 6. Spin density difference in (a) the $2 \times 2 \times 2$ _1Mn and (b) the $2 \times 2 \times 1$ _1Mn rutile supercells. Spin density difference is mainly attributed to the Mn–O(1) pairs.

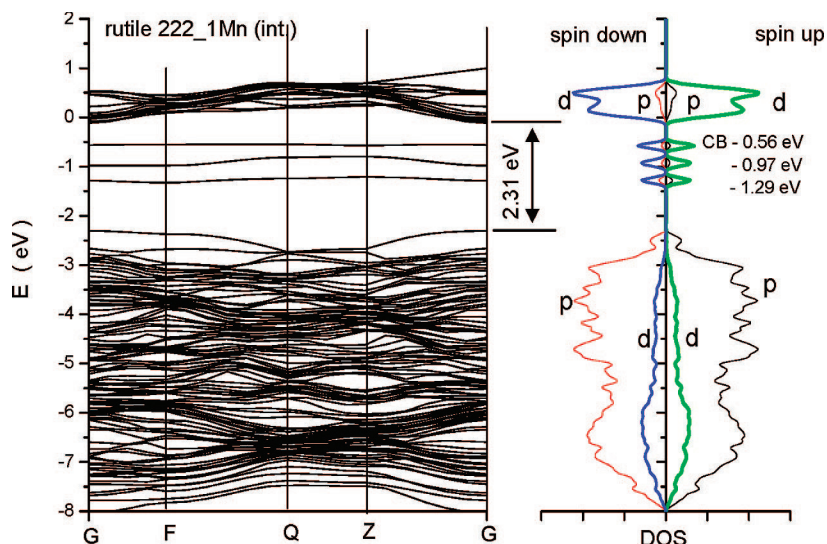


Figure 7. Band structure and partial DOS for the $2 \times 2 \times 2$ supercell containing an interstitial Mn atom, showing little magnetism. Localized defect levels, mainly attributed to the Mn 3d states, appear below the valence band.

effect in rutile energy gap due to Mn doping, with the intermediate bands/states from the up-spin states of the Mn 3d being shifted downward into deeper levels. Such a Hubbard U effect is only evident for intermediate states due to spin polarization.).

The spin polarization originates from the Mn–O bonds. For example, the spin density difference in the $2 \times 2 \times 2$ and $2 \times 2 \times 1$ supercells are shown in Figure 6, which reveals that the spin density difference is associated mainly with the nearest Mn–O(1) pairs. The values of magnetic moment due to spin polarization for the substitutionally doped rutile are summarized in Table 2. The considerable spin polarization due to Mn replacement of Ti is suggestive of potential spintronic applications, making use of substitutional Mn doping. Energetically, the spin-polarized state is more stable than the nonpolarized state, with the energy change due to ferromagnetic (FM) ordering being -0.04 , -0.03 , and -0.02 eV, for the substitutionally doped $2 \times 2 \times 1$, $2 \times 2 \times 2$, and $2 \times 2 \times 3$ supercells. Assigning parallel and antiparallel spins for the Mn atoms in a $2 \times 2 \times 1$ _2Mn supercell, one finds that the antiferromagnetic (AFM) state is only slightly favored over the ferromagnetic one (energy difference less than 0.0003 eV/atom), indicating the readiness for magnetic ordering in both FM and

AFM ways. This is consistent with recent experimental observation of room temperature ferromagnetism in Mn doped rutile phase.^{32–34}

3.3. Effect of Interstitial Mn Defect. Rutile TiO_2 tends to be reduced with deficiency in oxygen.²⁰ For the case of Mn doping, such oxygen deficiency can be in the form of either oxygen vacancy, or interstitial Mn in the octahedral centers of Ti cages, Figure 1d. The band structure of a $2 \times 2 \times 2$ supercell containing an interstitial Mn atom is shown in Figure 7. Into the energy gap, localized energy states are introduced by the interstitial Mn defect. The VB is shifted downward and the Fermi level cuts slightly into the bottom of the CB. The overall energy gap increases for 0.28 eV from 2.03 to 2.31 eV, with localized defect levels being 0.56, 0.97, and 1.29 eV below CB. Detailed analysis of atomic density of states shows that these defect levels are attributed mainly to the Mn 3d states. While these localized states can contribute to redshift for charge carrier generation under visible photon radiation, the mobility of carrier in the localized states is implicated. Electrons that are excited from the VB to these localized states will not be contributing to electron conductivity, and they have to wait for secondary excitation to the CB to take part in the PV energy conversion.

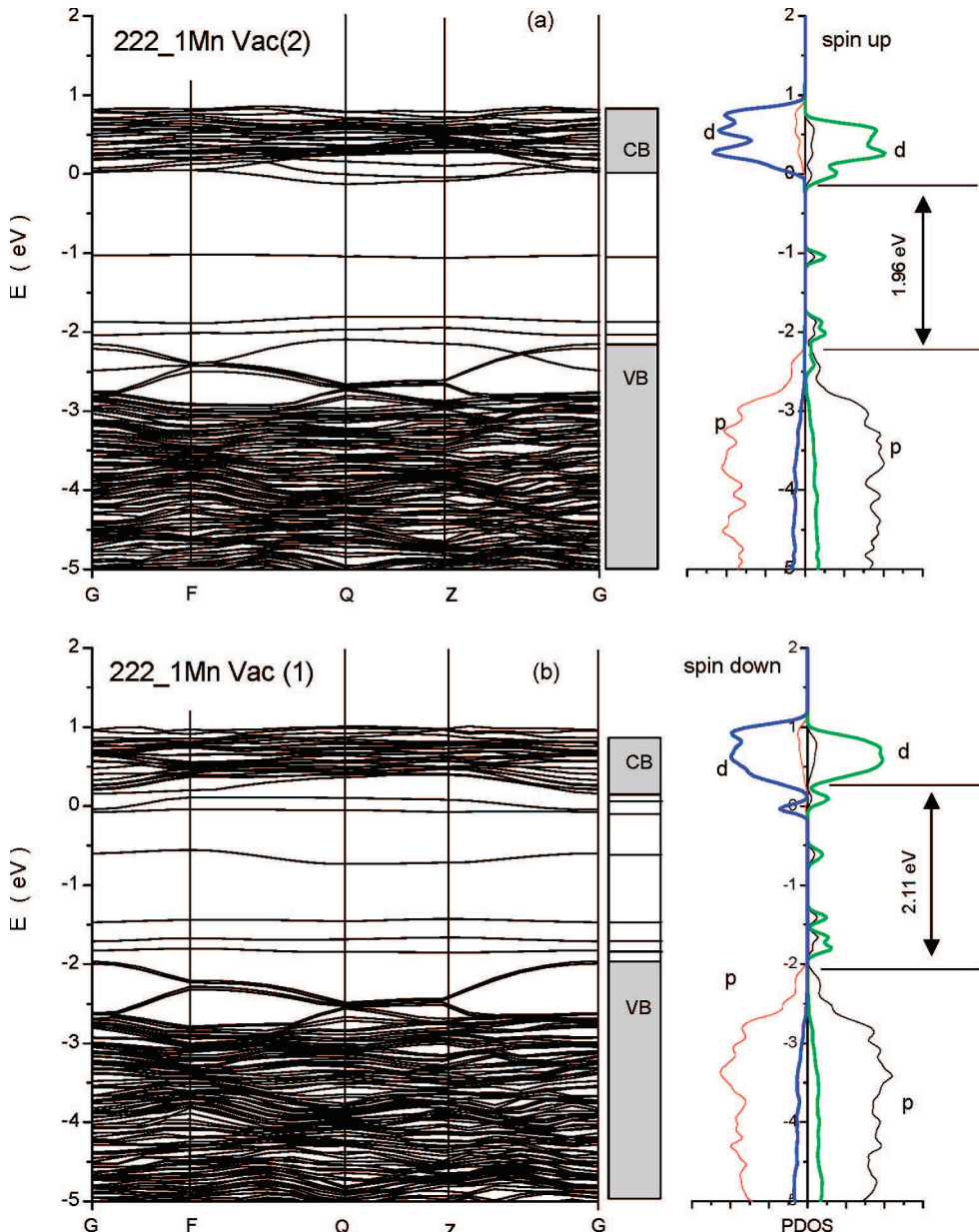


Figure 8. Band structure of the $2 \times 2 \times 2$ _1Mn supercell associated with a vacancy: (a) vacancy at O(2) position, and (b) vacancy at O(1) position. Localized defect levels exist in the forbidden bands. The band gaps for (a) and (b) are 2.11 and 1.96 eV, respectively. The right panel show PDOS of the corresponding band structure. The defect levels are indicated between the forbidden bands in the middle, which are attributed to the Mn d and as well as O p states.

This makes the interstitial defect less desirable for photonic or photovoltaic purposes.

The spin density difference associated with the interstitial Mn is negligible, and little spin polarization can be achieved. This can be analyzed in line with the structural configuration, where the interstitial Mn atom is also bonded to Ti atoms at the corners of an octahedral cage. In such a structural configuration, the number of nearest O neighbors to Mn is reduced from four to two, and the Mn–O bonding is significantly weakened, leading to considerably enlarged bond lengths with respect to that of the substitutional Mn. Such weakened O–Mn(int.) bonding makes the nearest bond length even greater than that for the second nearest of the substitutional Mn in the $2 \times 2 \times 2$ supercell (1.957 vs 1.944 Å), and the second O–Mn(int.) bond length reaches as large as 2.034 Å (Figure 8). As is discussed in the previous section, spin polarization is associated with strong bonding between Mn and O, especially the nearest

Mn–O(1) bond for the substitutional Mn. Such strong bonding is not associated with the interstitial Mn atom. It is worth pointing out that due to the remarkable difference in spin polarization, the substitutional and interstitial doping states of Mn are likely distinguishable by nuclear magnetic resonance measurement. This could be the working basis for using a new technique to characterize the chemical state of Mn in doped rutile, offering key information for material quality to device engineers.

The energy of formation for such a defected structural configuration is nearly the same as that for the substitutional case (Table 2), suggesting the thermodynamic readiness for the existence of interstitial Mn, when oxygen deficiency occurs. This is consistent with the fact that oxygen deficiency is typical in natural rutile.²⁰ In order to eliminate the interstitial Mn defect, oxygen deficiency should be avoided or corrected during

materials processing. This will be further elaborated in the following Section 3.4.

3.4. Effect of Oxygen Vacancy Associated with Mn Dopant. The effect of oxygen vacancy associated with Ti atoms in rutile was studied by previous researchers.^{16,19} We thus focus on oxygen vacancies in the nearest and second nearest neighborhood of substitutional Mn atoms. For a $2 \times 2 \times 2$ supercell containing an oxygen vacancy at the nearest (vac_1) and second nearest neighborhood (vac_2) of a substitutional Mn (Figure 1d), band structure calculations reveal many a localized defect level in the forbidden band. In the case of vac_1, there are six defect levels below CB or above VB (CB-0.10, CB-0.21, CB-0.82, VB+0.16, VB+0.28, VB+0.52). An oxygen vacancy at vac_2 induces four defect levels (CB-0.13, CB-0.82, VB+0.22, VB+0.55).

Interestingly, the energy of formation of these two types of oxygen vacancies is nearly the same, with that for vac_1 only 0.01 eV/atom higher than that for vac_2. The energy of formation of oxygen vacancy is dependent on the supercell sizes and associated vacancy contents. For a $2 \times 2 \times 2$ supercell, the energy of formation for vac_1 associated with Ti is 0.91 eV/atom, while the corresponding vacancy formation energy associated with Mn is only slightly smaller (0.906 eV/atom). This is also comparable to theoretical values for the corresponding oxygen vacancy in anatase (0.97 eV/atom³⁵).

The appearance of localized defect levels due to oxygen deficiency at the neighborhood of substitutional Mn atoms are more complex than oxygen vacancies associated with Ti atoms,^{16,19} the latter only inducing one defect level below CB. Such defect levels due to oxygen deficiency are consistent with the experimentally observed coloring due to the reduction of rutile TiO₂.²⁰ Experimental measurements showed that vacancy-induced states in pure rutile are 0.75–1.18 eV below CB,³⁶ which corresponds to 25–40% of the energy gap.

It is worth pointing out that the existence of defect levels, either due to interstitial Mn atoms or oxygen vacancies, may be useful to photocatalytic applications. They may not be as useful to the photovoltaic application, where carrier mobility plays an important role. Fortunately, due to the high oxygen affinity of transition metals, such a problem could be overcome by thermal treatment in an oxygen environment, i.e., calcination. The current theoretical finding is consistent with experimental observations that calcination was found to be extremely important for effective redshift in ion implanted TiO₂.^{4,22} The effect of calcination is therefore attributed to the elimination of the oxygen deficiency defects, associated either with interstitial Mn or with oxygen vacancies, leading to tidier band structures free of localized states inside the energy gap. The same care should be taken to eliminate the oxygen deficiency defects, when other processing techniques (e.g., codeposition) are used, in order to exploit the full potential of Mn doping for the reduction of energy gap of rutile TiO₂.

As to spin polarization, oxygen vacancies associated with substitutional Mn atoms enhances the magnetic moment (Table 2). For the $2 \times 2 \times 2$ supercell having oxygen vacancy at the vac_1 position associated with the substitutional Mn, the magnetic moment is increased from 3.4406 to 3.9728. The vac_2 configuration is particularly effective, increasing the magnetic moment for 45% up to 5.0056. Therefore, oxygen deficiency may be useful for spintronic applications of Mn doped rutile, while there might be some practical complications for their association with substitutional Mn.

The exploration of spintronics in semiconductor materials is attracting extensive research interest, since either adding the

spin degree freedom to conventional charge-based devices or using spin alone has great potential advantages of nonvolatility and increased integration densities with respect to conventional semiconductor devices.³⁷ The results of this work indicate the likely potential in using substitutional Mn doping for applications such as nonvolatile random access memory (NVRAM).

4. Conclusions

Substitutional Mn doping at the Ti site is effective to reduce the energy gap of rutile TiO₂, with redshift significantly enhanced through increased Mn doping level. Intermediate energy bands are introduced into the forbidden bands, at moderate doping levels. The up spin states of the Mn 3d electrons dictate the effects on energy gap reduction. Replacing the Ti lattice site by Mn has the potential to narrow the rutile energy gap into the red or even infrared spectral regime of solar radiation.

Spin polarization occurs when rutile is doped with substitutional Mn at the Ti lattice sites, with spin density difference being associated with Mn–O bonds. However, little spin polarization is associated with interstitial Mn atoms. Such correlation of spin polarization to the chemical state of the Mn dopant may be the working basis to use NMR for the characterization of the quality of doped rutile phase. Doping rutile at the Ti lattice sites may thus be useful for spintronic applications. Oxygen vacancies associated with the substitutional Mn atom may be useful in enhancing the magnetic moment. The results of this work indicate the likely potential in using substitutional Mn doping for applications such as nonvolatile random access memory.

Localized levels are associated with defects due to oxygen deficiency, i.e. interstitial Mn atoms and oxygen vacancies. Their existence may not be helpful for effective redshift of the rutile energy gap and they need to be eliminated during materials synthesis of device fabrication. Calcination of implanted materials is a way to serve for such a purpose.

Acknowledgment. Financial support from the Joule Centre under the contract JIRP 306/04 is acknowledged.

References and Notes

- (1) O'Regan, O.; Grätzel, M. *Nature* **1991**, *353*, 737.
- (2) Kay, A.; Grätzel, M. *Sol. Energy Mater. Sol. Cells* **1996**, *44*, 99.
- (3) Morrison S. R. *Electrochemistry at Semiconductor and Oxidized Metal Electrodes*; Plenum Press: New York, 1980.
- (4) Meng, Ni; Michael, K.H. Leung; Dennis, Y. C.; Leung, Sumathy K. *Renewable Sustainable Energy Rev.* **2007**, *11*, 401.
- (5) Ollis D. F.; Al-Ekabi H. *Photocatalytic Purification and Treatment of Water and Air*; Elsevier: Amsterdam, 1993.
- (6) Hoffmann, M. R.; Martins, S. T.; Choi, W.; Bahnmann, D. W. *Chem. Rev.* **1995**, *95*, 69.
- (7) An-Wu, Xu; Yuan, Gao; Han-Qin, Liu J. *Catal.* **2002**, *207*, 151.
- (8) Burdett, J. K.; et al., *J. Am. Chem. Soc.* **1987**, *109*, 3639.
- (9) Tang, H.; Le'vy, F.; Berger, H.; Schmid, P. E. *Phys. Rev. B* **1995**, *52*, 7771.
- (10) Kesong, Yang; Ying, Dai; Baibiao, Huang J. *Phys. Chem. C* **2007**, *111*, 12086.
- (11) Lan, Mi; Peng, Xu; Hong, Shen; Pei-Nan, Wang; Weidian, Shen *Appl. Phys. Lett.* **2007**, *90*, 171909.
- (12) Cristiana, Di Valentini; Emanuele, Finazzi; Gianfranco, Pacchioni; Annabella, Selloni; Stefano, Livraghi; Maria Cristina, Paganini; Elio, Giambello *Chem. Phys.* **2007**, *339*, 44.
- (13) Frédéric, Labat; Philippe, Baranek; Christophe, Domain; Christian, Minot; Carlo, Adamo *J. Chem. Phys.* **2007**, *126*, 154703.
- (14) Kesong, Yang; Ying, Dai; Baibiao, Huang J. *Phys. Chem. C* **2007**, *111*, 18985.
- (15) Nicholas, C. Wilson; Ian, E. Grey; Salvy, P. Russo *J. Phys. Chem. C* **2007**, *111*, 10915.
- (16) Eunae, Cho; Seungwu, Han; Hyo-Shin, Ahn; Kwang-Ryeol, Lee; Seong, Keun Kim; Cheol, Seong Hwang *Phys. Rev. B* **2006**, *73*, 193202.

- (17) Glassford, K. M.; Chelikowsky, J. R. *Phys. Rev. B* **1992**, *46*, 1284.
- (18) Lee, C.; Ghosez, P.; Gonze, X. *Phys. Rev. B* **1994**, *50*, 13379.
- (19) Islam, M. M.; Bredow, T.; Gerson, A. *Phys. Rev. B* **2007**, *76*, 045217.
- (20) Cronemeyer, D. C. *Phys. Rev.* **1959**, *113*, 1222.
- (21) Anpo, M.; Takeuchi, M. *J. Catal.* **2003**, *216* (1–2), 505.
- (22) Dvoranová, D.; Brezová, V.; Mazúr, M.; Malati, M. *A. Appl. Catal., B* **2002**, *37*, 91.
- (23) Kohn, W.; Sham, L. *J. Phys. Rev.* **1965**, *A140*, 1133.
- (24) Clark, S. J.; Segall, M. D.; Pickard, C. J.; Hasnip, P. J.; Probert, M. J.; Refson, K.; Payne, M. C. Z. *Kristallogr.* **2005**, *220* (5–6), 567–570.
- (25) Vanderbilt, D. *Phys. Rev. B* **1990**, *41*, 7892.
- (26) Wu, Z.; Cohen, R. E. *Phys. Rev. B* **2006**, *73*, 235116.
- (27) Perdew, J. P.; Burke, K.; Ernzerhof, M. *Phys. Rev. Lett.* **1996**, *77*, 3865–3868.
- (28) Monkhorst, H. J.; Pack, J. D. *Phys. Rev. B* **1977**, *16*, 1748.
- (29) Gale W. F.; Totemeier T. C., Eds. *Smithells Metals Reference Book*, 8th ed.; Elsevier: New York, 2004.
- (30) Gray D. E., Ed. *American Institute of Physics Handbook*; McGraw-Hill: New York, 1972.
- (31) Villars P., Calvert, L.D., Ed. *Pearson's Handbook of Crystallographic Data for Intermetallic Phases*, 2nd ed.; ASM International: Materials Park, OH, 1991.
- (32) Xu, I. M.; Yu, Y. P.; Xing, X. J.; Wu, X. Y.; Li, S. W. *Appl. Phys. A: Mater. Sci. Process.* **2008**, *92*, 361.
- (33) Kim, K. J.; ParkY.R.; LeeJ.H.; Choi, S. L.; Lee, H. J.; Kim, C. S.; Park, J. Y. *J. Magnet. Magnet. Mater.* **2007**, *316*, e215.
- (34) Sangaletti, L.; Mozzati, M. C.; Galinetto, P.; Azzoni, C. B.; Speghini, A.; Bettinelli, M.; Calestani, G *J. Phys.: Condens. Matter* **2006**, *18*, 7643.
- (35) Cronemeyer, D. C. *Phys. Rev.* **1959**, *113*, 1222.
- (36) Na-Phattalung, S.; Smith, M. F.; Kim, K.; Du, M. H.; Wei, S. H.; Zhang, S. B.; Limpijumnong, S. *Phys. Rev. B* **2006**, *73*, 125205.
- (37) Wolf, S. A.; Awschalom, D. D.; Buhrman, R. A.; Daughton, J. M.; von Molnár, S.; Roukes, M. L.; Chtchelkanova, A. Y.; Treger, D. M. *Science* **2001**, *294*, 1488.

JP8043797